RSC Advances

PAPER

View Article Online
View Journal | View Issue

Cite this: *RSC Adv.*, 2020, **10**, 28567

Dye wastewater treatment enabled by piezo-enhanced photocatalysis of single-component ZnO nanoparticles†

Yothin Chimupala,[a] Chitsanupong Phromma,[a] Saranphong Yimklan,[b] Natthawat Semakul[b] and Pipat Ruankham*[cd]

Conventionally, composite materials are usually employed as a catalyst in piezo-photocatalytic dye wastewater treatment. Here, we report the synthesis of ZnO nanoparticles, as a single-component catalyst, by surfactant-assisted precipitation in which the size of ZnO nanoparticles (20–100 nm) can be simply controlled by the use of Tween80 as a surfactant. Although, ZnO nanoparticles exhibited appreciable photocatalytic activities for the degradation of methylene blue (MB) dye, upon the addition of a mechanical force, the photocatalytic dye degradation efficiency was substantially improved. Furthermore, we postulated that the surface properties of ZnO play an important role in charge transfer phenomena based on photoluminescence results together with functional groups on the surface of ZnO. In addition, application of single-component ZnO in piezo-promoted photocatalytic degradation of cationic and anionic dyes was accomplished. Our results regarding the behaviour of single-component ZnO nanoparticles under vibrational energy in addition to their conventional solar harvesting can provide a promising strategy for developing photocatalysts for practical wastewater treatment.

Received 29th May 2020
Accepted 24th July 2020

DOI: 10.1039/d0ra04746e

rsc.li/rsc-advances

Introduction

Zinc oxide (ZnO) is a multifunctional material which is extensively used in various applications due to its environmental friendliness and diverse properties.[1–3] The excellent properties and availabilities of morphological control on the nanoscale make ZnO an excellent material for optoelectronics,[4–6] piezoelectric,[7,8] nanosensors[9] as well as antibacterial applications.[10–12] Since ZnO provides a direct wide band gap, photocatalytic activity for application in the elimination of toxic chemicals is also feasible.[13,14] Morphology, surface properties and crystal defects are important factors for achieving excellent photocatalytic activity.[14–16] However, using a single-component photocatalyst is practically limited because the UV light can be screened by catalyst particles themselves,[17] and it has a competitive charge recombination process at a high rate due to inefficient charge separation and transport.[18]

How to enhance photocatalytic efficiency is the key for practical use of ZnO for dye degradation in wastewater treatment especially in large scale process. Dual energy harvesting in ZnO is one of effective strategies to increase the dye degradation performance. Beside the long-run development of ZnO as photocatalyst, the piezoelectric effect of ZnO has recently applied in wastewater treatment applications.[8,19,20] Due to its high effective piezoelectric coefficient d_{33} (especially for ZnO nanorods at 130 pm V^{-1} (ref. 21)), ZnO is one of dominated piezoelectric materials. By introducing mechanical energy, induced dipoles with positively and negatively charged surfaces are created. The electric polarization of dielectric materials significantly creates driving force for transport of free charge carriers to the surface and also facilitates interfacial energetic states.[20,22] Therefore, these phenomena support the reduction–oxidation of O_2 and H_2O molecules to form superoxide and hydroxyl radicals for dye degradation as also occurred in the photocatalysis.[23,24] Consequently, synergic piezo-promoted photocatalysis is a promising strategy for application in wastewater treatment.

Conventionally, composite catalysts are employed as multi-energy harvesting as piezo-enhanced photocatalysts *e.g.*, ZnO/TiO_2 core–shell nanofiber, FeS/ZnO nanowire, carbon/ZnO and CuS/ZnO nanowire.[25–29] The photocatalytic efficiency immensely depends on the electron and hole generations, the charge separation, the competitive recombination process, and charge transport along distance between free carriers and active surfaces.[30,31] These composite catalysts utilize the benefits of narrow-band-gap semiconductors for expanding light

[a]*Department of Industrial Chemistry, Faculty of Science, Chiang Mai University, Chiang Mai, 50200, Thailand*

[b]*Department of Chemistry, Faculty of Science, Chiang Mai University, Chiang Mai, 50200, Thailand*

[c]*Department of Physics and Materials Science, Faculty of Science, Chiang Mai University, Chiang Mai, 50200, Thailand. E-mail: pipat.r@cmu.ac.th*

[d]*Research Center in Physics and Astronomy, Faculty of Science, Chiang Mai University, Chiang Mai, 50200, Thailand*

† Electronic supplementary information (ESI) available. See DOI: 10.1039/d0ra04746e

absorption into the visible region and for separating the photogenerated electron–hole pairs by both built-in electric field at the interface[32] and driving force induced by piezoelectric effects. This strategy could efficiently enhance the dye degradation efficiency.

Beside the composite catalysts, which may be prepared by a complicated synthetic method, single-component ZnO nanoparticle catalyst can be a simpler alternative. This is because nanoparticle-based catalysts possessed shorter transit time to the active surface area within their lifetime, therefore, the charge recombination and energy loss are suppressed resulting in excellent photocatalytic activities.[33] The charge separation of photogenerated electron–hole pairs in nanoparticles can be enhanced by the addition of mechanical energy as mentioned above. Therefore, we speculate that the dye degradation efficiency can be improved by piezo-enhanced photocatalysis with single-component ZnO nanoparticle-based catalysts.

In this work, size-controllable ZnO nanoparticles can be simply synthesized by precipitation method with the assistance of Tween80 (TW) as a surfactant, yielding particle size of 20–100 nm. The photocatalysis and piezo-promoted photocatalysis of as-synthesized and calcined ZnO in methylene blue (MB) degradations were studied which reveal that surface defects related to photocatalysis and piezo-promoted photocatalysis and dye degradation mechanism. In addition, calcined ZnO catalyzed piezo-promoted photocatalysis was also effective for the degradation of rhodamine B (RhB) and thymol blue (TB). Our single-component ZnO nanoparticle-based catalyst is a simpler alternative for potential dual utilization of vibrational and solar energy to deal with wastewater problems.

Experimental methods

Chemicals

Zinc nitrate hexahydrate ($Zn(NO_3)_2 \cdot 6H_2O$) was purchased from Sigma-Aldrich. Potassium hydroxide (KOH, 85%) was purchased from RCI-Labscan. Polyoxyethylene sorbitan monooleate or TW was obtained from Sigma-Aldrich. All chemicals were used as-purchased without further purification. Deionized (DI) water was used as the solvent in all reactions.

Synthesis of ZnO powder

ZnO powder was synthesized by a precipitation method with TW as surfactant. TW was added to a solution of zinc nitrate hexahydrate (0.1125 mM, 80 mL) in DI-water at different TW/Zn^{2+} molar ratios (0, 0.05, 0.10, 0.20, 0.40, and 0.60). The solution was hold at 60 °C before addition of an aqueous KOH solution (0.45 M, 40 mL) with dosing time of 10 min. The mixture was kept stirring vigorously at 60 °C for 120 min to produce white precipitate. After centrifugation, the supernatant was discarded, and the precipitates were collected. Residue in the obtained particles were removed by using DI-water and ethanol. Finally, the resultant products were dried in an oven at 60 °C overnight to obtain the ZnO powder. Note that $ZnO_{TW\text{-}x}$ refers to the ZnO powder synthesized by using TW/Zn^{2+} molar ratio of x, where x is 0, 0.05, 0.10, 0.20, 0.40, or 0.60.

Characterization techniques

Field emission scanning electron microscope (FE-SEM, JEOL JSM-6335F) was used to investigate the morphology of the resultant products. X-ray diffractometer (XRD, Rigaku MiniflexII) was used to determine the crystal structure of the obtained powder. Transmission Electron Microscope (TEM, JEM 2010) along with selected area electron diffraction (SAED) technique was employed to investigate nanoparticles and confirm phase formation. Thermogravimetric analysis (TGA), undertaken using Thermo plus EV02 (Rigaku), was used to determine residual contents of the samples. Bruker Tensor 27 FT-IR instrument was used to record Fourier-transform infrared (FT-IR) spectra of the samples with KBr pellets (BDH, 98.5%) in the range of 400–4000 cm^{-1}. Particle surface area was evaluated by Brunauer–Emmett–Teller (BET) technique on Autosorb 1 MP, Quantachrome. Photoluminescence (PL) spectrometer (AvaSpec-ULS2048LTEC) integrated with Ocean optic LED light sources was used to collect PL spectra of the ZnO powder by using excitation wavelength of 345 nm and power of 20 μW.

Photocatalytic and piezo-promoted photocatalytic activities

The photocatalytic and piezo-promoted photocatalytic activities of the samples was determined by decomposition of MB. The ZnO powder with a given amount of 25 or 100 mg was mixed with 100 mL of an aqueous MB (5 ppm, 100 mL). The mixture was first sonicated in an ultrasonic bath (120 W, 40 kHz) for 2 min. To obtain adsorption–desorption equilibrium, the suspension was then stirred for 30 min under dark condition. For photocatalytic experiment, UVA light with peak wavelength of 365 nm and intensity of 940 μW cm^{-2} was exposed to the suspension with constant stirring. On the other hand, for piezo-promoted photocatalytic test, ultrasonic radiation (120 W, 40 kHz) was additionally applied to the samples. In both experiments, 5 mL aliquots were taken at certain intervals to evaluate the decomposition of MB. They were then centrifuged at 4000 rpm for 5 min to separate ZnO catalyst before UV-vis measurement of supernatants (Specord 50 plus). The amount of MB remaining in the solution was calculated by considering a C_t/C_0 ratio, where C_0 is the initial concentration of MB and C_t is the residual concentration after UV irradiation time of t. The C_0 and C_t concentrations were determined by using the absorbance at 665 nm. The piezo-promoted photocatalyzed degradation of RhB and TB were evaluated similarly to MB. The concentration of dye and catalyst dosage were set at 5 ppm and 1.00 g L^{-1} (200 : 1 by weight of ZnO : MB), respectively. The absorbance at 554, 433 and 596 nm were recorded for RhB, TB (at pH 7) and TB (at pH 12), respectively. Total Organic Carbon (TOC) was analyzed with AJ-Analyzer multi N/C 3100 using standard method 5310.

Results and discussion

Crystallinity and morphology

XRD analysis was performed to confirm crystalline phase purity of the white precipitates. The XRD patterns of these samples are shown in Fig. S1 (ESI†). It is seen that the XRD peaks of all

samples at 31.8°, 34.4°, 36.2°, 47.5°, and 56.6° are corresponding to the reflection from (100), (002), (101), (102), and (110) planes of the ZnO wurtzite structure (JCPDS 36-1451). In addition, there is no characteristic peak of other impurities or intermediate species. These characteristics imply that only single-phase ZnO was synthesized by our method.

The grain size and morphology of the ZnO powder were observed by using FE-SEM technique. The observed images are demonstrated in Fig. 1. The grain size of the particles was determined by using ImageJ software. It was found that the average grain size of ZnO powder prepared by a conventional precipitation method is approximately 235 nm with standard deviation (SD) of 87 nm (see ESI† for particle size distribution in Fig. S2,† lattice parameters and crystallite size in Table S1†). By adding TW at molar ratio of 0.05, the grain size of $ZnO_{TW\text{-}0.05}$ nanoparticles significantly decreased to 92 nm (SD = 32 nm). The smallest average grain size of about 40 nm (SD = 10 nm) was obtained with $ZnO_{TW\text{-}0.20}$. It is likely that no more reduction of grain size is observed even though the amount of TW was increased to 0.40 and 0.60 (as seen in Fig. S3† in ESI†). Therefore, the investigated results suggest that the 0.20 molar ratio is the optimum value for size reduction. Non-ionic surfactant TW was employed as the directing agent for the formation of ZnO nanoparticles. Dispersion of TW in the aqueous solution forms the micellar structures in which the hydrophobic tails reside inside the micellar core while hydrophilic heads point toward the aqueous solution (see ESI, Fig. S4†). The hydrophilic heads contain several hydroxyl and polyether which functions as a chelating ligand for Zn^{2+} ions. Consequently, the size of micelle plays an important role in the size of ZnO nanoparticle. After the addition of base, OH^- ions react with Zn^{2+} ions to form zinc hydroxide in which the precipitation occurs when the pH value reaches the stoichiometric amount for the precipitation. Subsequently, heating the solution at 60 °C leads to the formation of ZnO nanoparticles.

TEM observation and SAED technique were carried out for further examining the particle size and crystallinity of $ZnO_{TW\text{-}0.20}$ nanoparticles. The TEM image and the SAED pattern are shown in Fig. S5 (see ESI†). It is seen that the average primary particles size observed by TEM technique is at 25 nm (SD = 11). This value is slightly smaller than that of the one observed by FE-SEM technique due to the edges of the particles were more clearly visible in the images system leading to higher accuracy in measurement of primary particles size. Moreover, SAED pattern from a group of particles reveals ring spacing characteristics of ZnO wurtzite structure for (100), (002), (101), (102), and (110) planes. The SAED analysis confirmed the crystal structure as examined by XRD.

Surface properties

FT-IR was carried out to observe the surface properties of the synthesized ZnO powders ($ZnO_{TW\text{-}0}$, $ZnO_{TW\text{-}0.20}$, and $ZnO_{TW\text{-}0.60}$) in comparison with pure TW as shown in Fig. 2. The bands at 1358 cm^{-1} and 1460 cm^{-1} in the FT-IR spectrum of pure TW are accounted for symmetrical and asymmetrical bending of $-CH_3$, respectively. While, the asymmetrical and symmetrical stretching vibrations of $-CH_2-$ correspond to the bands at 2920 cm^{-1} and 2856 cm^{-1}, respectively.[34] For all ZnO_{TW} samples, the broad bands at approximately 3383 cm^{-1} and the small peaks at 1641 cm^{-1} which is owing to surface O–H stretching and C=O stretching, respectively.[35,36] Furthermore, the band at 1384 cm^{-1} refers to the asymmetric stretching of C=O from the ester group (–COO–).[11,37] On the other hand, the characteristic wavenumber of 420 cm^{-1} was observed which is ascribed to Zn–O stretching.[36,37] This observation implies that the adsorption of TW on the surface of ZnO nanoparticles is negligible.

Thermogravimetric analysis (TGA) curves (see Fig. S6 in ESI†) reveal that organic residues existed in the ZnO, $ZnO_{TW\text{-}0.20}$, and $ZnO_{TW\text{-}0.60}$ samples for 3.08%, 3.77%, and 4.09% by weight, respectively. These values imply that $ZnO_{TW\text{-}0.60}$ contains slightly higher amount of residue comparing to $ZnO_{TW\text{-}0.20}$ (4.09–3.77 = 0.32%) and ZnO (4.09–3.08 = 1.01%), respectively. The higher residue amount is attributed to larger molar percentage of TW molecules during the synthesis. Since particle size of those samples observed by FE-SEM (Fig. 1d and f) does

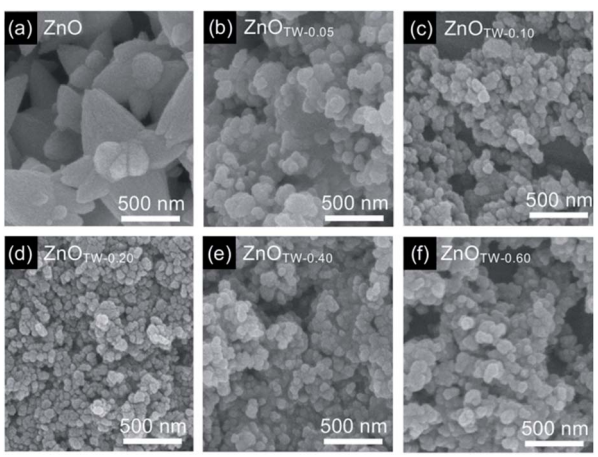

Fig. 1 FE-SEM images of the ZnO nanopowder synthesized by using TW/Zn^{2+} molar ratio at (a) 0, (b) 0.05, (c) 0.10, (d) 0.20, (e) 0.40, and (f) 0.60.

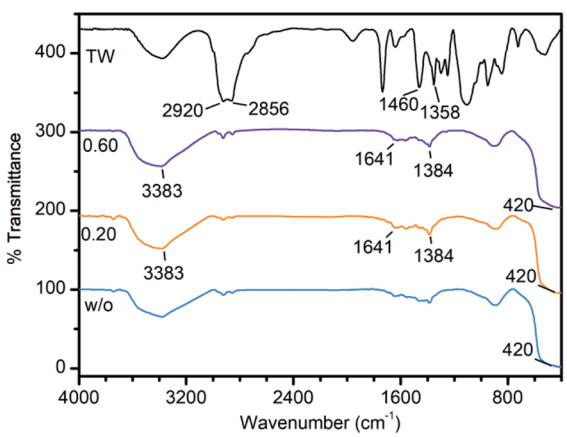

Fig. 2 FT-IR spectra of pure TW and ZnO nanopowder synthesized using TW/Zn^{2+} with molar ratio at 0, 0.20, and 0.60.

not show significant difference, $ZnO_{TW-0.20}$ is chosen for further investigation and application as single-component catalyst. The nitrogen adsorption–desorption isotherms analyzed by BET analysis for ZnO_{TW-0} and $ZnO_{TW-0.20}$ nanoparticles are presented in Fig. S7† (see ESI†). The observed isotherms of ZnO_{TW-0} and $ZnO_{TW-0.20}$ are corresponded to non-porous materials due to their low N_2-absorbed volume even relative pressure reached a point of 0.95. However, $ZnO_{TW-0.20}$ can also have the pore size distribution in the macropore region due to the intraparticular void generated from agglomeration and aggregation phenomena of nanoparticles which are measured above the relative pressure of 0.95. Therefore, the synthesized ZnO nanopowder is non-porous materials. In addition, it was found that the $ZnO_{TW-0.20}$ achieved a BET surface area of 29.9 $m^2\ g^{-1}$, which is significantly higher than that of the ZnO_{TW-0} (9.3 $m^2\ g^{-1}$). This characteristic can be explained by the different in particle size as monitored by FE-SEM images in Fig. 1. Accordingly, the above analyses indicate that the use of TW molecules in a precipitation method can reduce the particle size of ZnO with organic residues of less than 5% by weight and significantly increase the BET surface area.

Photocatalytic activities of $ZnO_{TW-0.20}$ nanoparticles

$ZnO_{TW-0.20}$ nanoparticles were selected as single-component catalyst for photodegradation of MB due to their excellent surface properties among the ZnO and ZnO_{TW-60} as mentioned above. The ZnO catalyst dosages of 0.25 and 1.00 g L^{-1} (50 : 1 and 200 : 1 by weight of ZnO : MB, respectively) was used for initial aqueous MB solution of 5 ppm. The normalized concentration of MB in the presence of $ZnO_{TW-0.20}$ was plotted against UV irradiation time in Fig. 3. There is no significant photodegradation of MB molecules for the solution without ZnO catalyst under UV irradiation for 120 min. As seen in Fig. 3a, the as-synthesized $ZnO_{TW-0.20}$ nanoparticles with dosages of 0.25 g L^{-1} showed significant photodegradation in comparison with the one without catalyst. However, with increasing dosage to 1.00 g L^{-1} provides slightly higher photocatalytic activity than dosage of 0.25 g L^{-1}. Even though the amount of catalyst was increased, there was no dramatic change in photodegradation. This phenomenon may be explained by the surface defects of ZnO nanoparticles (as observed by FT-IR and TGA analyses) which may serve as surface recombination centers for photogenerated electrons and holes, causing less hydroxyl radical formation.[33]

In order to remove the surface residues on the catalyst, the $ZnO_{TW-0.20}$ powder was calcined at 600 °C for 1 h. At such temperature, most of organic residuals were efficiently removed as confirmed by TGA analysis (Fig. S6†). Comparing the photocatalytic properties of the as-synthesized $ZnO_{TW-0.20}$ nanoparticles, the calcined $ZnO_{TW-0.20}$ catalyst achieved significant change in photodegradation of MB as seen in Fig. 3b. Especially, for calcined $ZnO_{TW-0.20}$ with dosage of 1.00 g L^{-1}, the residual MB concentration at 120 min was approximately half of the non-calcined one at the same conditions. These results suggested that our $ZnO_{TW-0.20}$ nanoparticles present the photocatalytic activity and the photodegradation efficiency can be enhanced by calcination of the ZnO nanopowder.

In order to get insight into the effects of calcination on semiconducting properties, various spectroscopic techniques were carried out. PL spectra was recorded at room temperature to evaluate surface and native defects of the as-synthesized $ZnO_{TW-0.20}$ and the calcined one. By using excitation wavelength of 345 nm, a band in the ultraviolet emission (370–400 nm) and a broadband in the visible region (400–700 nm) were observed. The experimental PL spectra were fitted with Voigt function and they were well divided into several curves as seen in Fig. 4. The PL emissions of the as-synthesized $ZnO_{TW-0.20}$ can be seen in four different peaks (P1–P4), while the calcined $ZnO_{TW-0.20}$ show only three peaks (P1–P3). The UV peak (P1) is related to near-band-edge (NBE) emissions which concern emissions of free exciton (FX), bound exciton (BX) and their corresponding phonon replicas.[38–41] Red spectral shift (10 nm) and reduction in intensity for P1 peak were revealed after calcination. These behaviors were observed in some cases for

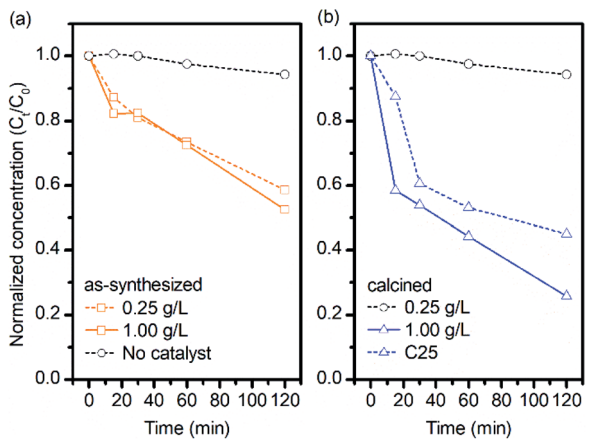

Fig. 3 Photodegradation efficiency of MB solutions in 0.25 g L^{-1} and 1.00 g L^{-1} mixtures of (a) as-synthesized $ZnO_{TW-0.20}$ and (b) calcined $ZnO_{TW-0.20}$ under exposure to UV light.

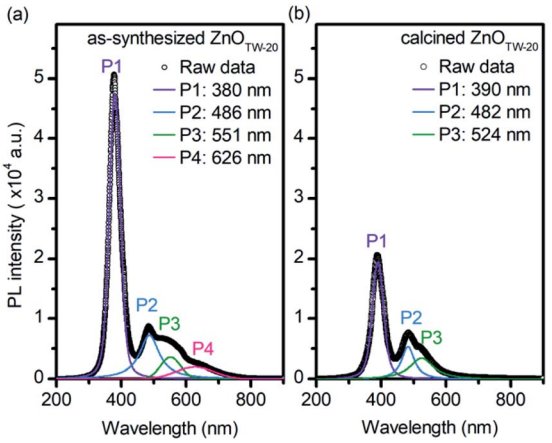

Fig. 4 Room temperature PL spectra of (a) as-synthesized $ZnO_{TW-0.20}$ and (b) calcined $ZnO_{TW-0.20}$. The experimental raw data and the fitted curves are represented by open circles and solid lines, respectively.

post treatment of ZnO at high temperature.[42–44] The spectral shift could not be related to the quantum confinement effect since the particle size of the $ZnO_{TW-0.20}$ is much larger than the Bohr radius of ZnO (2.34 nm).[45] However, possible reasons behind this spectral shift could be either different concentration of native defects[38,41] in the calcined $ZnO_{TW-0.20}$ or variation in electron-phonon coupling[38,46] after calcination.

On the other hand, blue (P2), green (P3), and orange-red (P4) emissions of ZnO have been well described by various reports.[41,47,48] The blue P2 peak is often corresponded to oxygen vacancies[49] or Zn interstitials[47] which are the native defects of ZnO. The green P3 emission is attributed to the singly ionized oxygen vacancies.[41,47] Both blue and green emissions were observed in the as-synthesized $ZnO_{TW-0.20}$ and the calcined sample with comparable peak intensities, implying that the calcination did not significantly affect the presence of native defects. However, the orange-red P4 peak disappeared in the PL spectra of calcined $ZnO_{TW-0.20}$. The orange-red emission was ascribed to the excess oxygen on the ZnO surface, which relates to the surface modifications and heat treatment.[41,43,50] The observed behavior implies that the surface residuals of $ZnO_{TW-0.20}$ was efficiently removed by the calcination as also confirmed by the TGA (Fig. S6†).

Bright-field TEM and FE-SEM observations were also used to investigate the particle morphology and size of the calcined $ZnO_{TW-0.20}$ nanoparticles as demonstrated in Fig. 5. Calcination at 600 °C does not only remove organic residuals on the surfaces but also improve uniformity. After the calcination, the change from irregularly equiaxed grain (Fig. 1d) to a homogeneously spherical morphology (Fig. 5a) was observed. In addition, average grain size of calcined sample is increased (58 nm SD = 15 nm *vs.* 40 nm, SD = 10 nm for uncalcined). It was found that the calcination did not significantly affect the crystallinity as shown in Fig. 5a. The calculated crystallite size of calcined sample is negligible (see Table S1 in ESI†). Altogether, these results suggested that surface organic group creates surface trap as indicated by PL results. These centers increase the possibility for charge recombination and obstructs the contact of reactants and photogenerated charge carrier on catalyst surface.[51]

Piezo-promoted photocatalytic activities of $ZnO_{TW-0.20}$ nanoparticles

Further improvement in the degradation of MB was performed by applying ultrasonic wave to promote the excitation of excitons and dynamics of photogenerated electrons and holes. The piezo-promoted photocatalysis of both as-synthesized $ZnO_{TW-0.20}$ and calcined $ZnO_{TW-0.20}$ under ultrasonic radiation and UV light is seen in Fig. 6. In addition, the rate constant (k) in photocatalysis and piezo-photocatalysis were determined as shown in Table S3 (see ESI†). As-synthesized $ZnO_{TW-0.20}$ catalyst shows the degradation of MB at catalyst dosages of 1.00 g L^{-1} (200 : 1 by weight) faster than that of 0.25 g L^{-1} (50 : 1 by weight). These results indicate that catalyst dosage of 200 mg spends at the minimum of 120 min to degrade 1 mg of MB. It should be noted that the surface area is increased as the catalyst dosage increased. However, the interparticular quenching between piezo-induced positive charge and negative charge[52] dominates over the higher active surface area.

In addition, comparing the photodegradation efficiency of the as-synthesized $ZnO_{TW-0.20}$ in the absence (Fig. 3a) and presence (Fig. 6a) of ultrasonic wave, MB was more efficiently degraded under dual ultrasonic and UV stimulation at both catalyst dosages. These characteristics may be explained by an increase in photogenerated electrons and holes due to piezoelectric-driven internal field.[20,22] The internal field, generated by photoelectric effect under the presence of ultrasonic

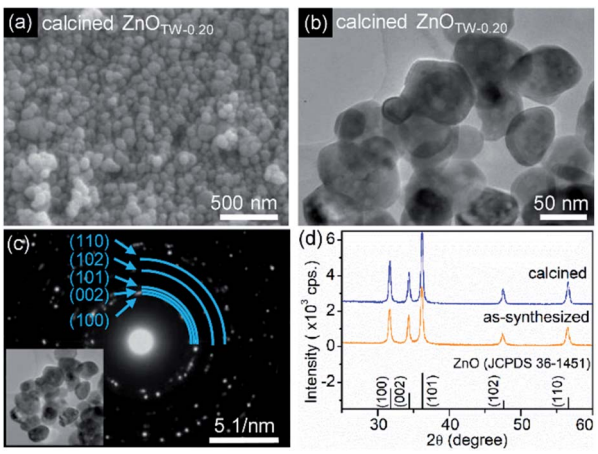

Fig. 5 (a) A SEM image of the calcined $ZnO_{TW-0.20}$, (b) a bright field TEM image taken from the calcined $ZnO_{TW-0.20}$, (c) a diffraction pattern of a group of calcined $ZnO_{TW-0.20}$ particles shown in the image inset (d) XRD patterns of calcined $ZnO_{TW-0.20}$ and as-synthesized $ZnO_{TW-0.20}$.

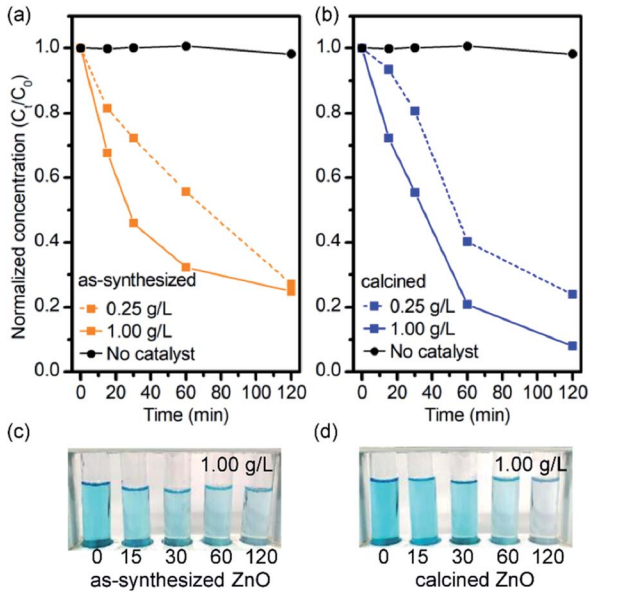

Fig. 6 Piezo-promoted photodegradation efficiency of MB solutions in 0.25 g L^{-1} and 1.00 g L^{-1} mixtures of (a) as-synthesized $ZnO_{TW-0.20}$ and (b) calcined $ZnO_{TW-0.20}$ under ultrasonic radiation and UV light with their optical images of MB in 1.00 g L^{-1} mixtures solution in (c) and (d), respectively.

wave, promotes the charge extraction of photogenerated excitons into free electrons and free holes. Then, these free charge carriers move to the respective charged surfaces for reduction-oxidation of O_2 and H_2O molecules. Therefore, this behavior could reduce the drawbacks of ZnO surface residuals as mentioned above and enhance the reaction rate at the beginning. The mechanical force is even more pronounced in the case of the calcined $ZnO_{TW\text{-}0.20}$ in which provided significantly higher degradation efficiency than that of the as-synthesized catalyst. The rate constant of as-synthesized catalyst is inferior to calcined catalyst with the same dosage (Fig. 6b) although they possessed higher surface area (see Table S2†). This result may be explained by drawbacks of surface residuals in as-synthesized catalysts. Therefore, mechanical force can improve MB degradation under photocatalytic even the low catalyst loading and shorter reaction time.

After having established piezo-promoted photocatalyst for the degradation of MB as a representative of small molecule cationic dye, the generality of the degradation by catalyst to other dyes was further investigated. Therefore, RhB and TB were selected as a candidate for large molecule cationic dye and anion dye, respectively. Piezo-enhanced photocatalytic degradations of RhB and TB with calcined $ZnO_{TW\text{-}0.20}$ are illustrated in Fig. 7. Significant ZnO catalyzed degradation of RhB was found with almost 90% degradation. While the ZnO catalyzed degradation of TB is slightly less effective (*ca.* 81% degradation). It should be noted that the TB degradation of 48% was also found in the control experiment suggesting the photolysis of TB. In addition, due to the overlapped absorption of TB and residual ZnO, pH of photodegraded TB solution was adjusted from 7 to 12, resulting in the color changes from yellow to blue.

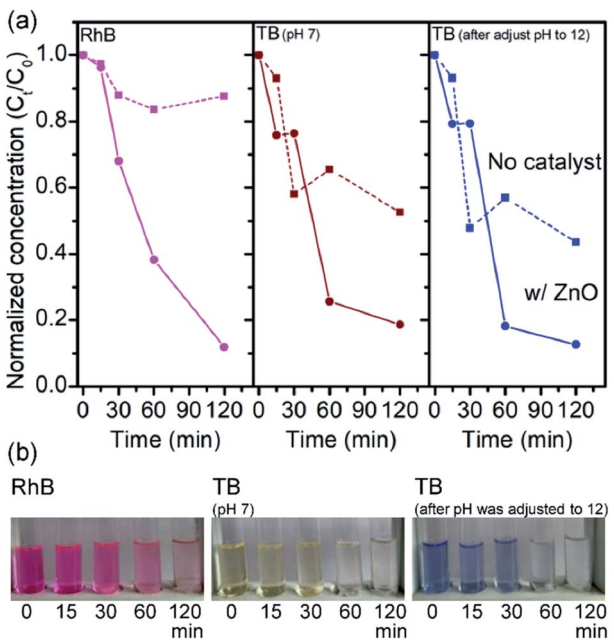

Fig. 7 (a) Piezo-promoted photodegradation of RhB, TB at pH 7, and the photodegraded TB solution after pH was adjusted to 12 with their corresponding optical images in (b).

The C_t and C_0 values of TB could be determined from the absorbance at 596 nm. The normalized concentration of TB obtained after pH adjustment to 12 was consistent to the one of pH at 7 as seen in Fig. 7. According to the MB degradation in Fig. 6b, the degradation efficiency of RhB and TB is comparable to that of MB within 2 hours (Table S4†). Therefore, ZnO effectively catalyzed the degradation of cationic and anion dyes *via* piezo-enhanced photocatalysis. The decolorization of organic dyes may not imply that the dye is completely degraded into CO_2 and H_2O. TOC values related to the total concentration of organic content in the solution and reflects the degradation efficiency of the photocatalytic process. After the complete decolorization of the solution, the TOC values slightly decreased (Table S4†). This result suggests that the products obtained from the piezo-promoted photocatalytic process presumably are CO_2, small organic molecules and degraded dyes.

This work demonstrated that ZnO nanoparticles obtained from TW-assisted precipitation exhibited appreciable organic-dye degradation efficiency under piezo-promoted photocatalysis. Dye degradation efficiencies are comparable to ones reported by other previous works as shown in Table S5.† In addition, this work also highlights the merit of single-component catalyst and simple synthetic method which is alternative to other complex synthetic processes.

Dye degradation mechanisms

The mechanism of piezo-enhanced photocatalytic degradation of organic dyes by ZnO nanoparticles are tentatively proposed in Fig. 8. When UV light irradiates to ZnO semiconductors, excited electrons at the conduction band (CB) and holes at the valence band (VB) are created (Fig. 8a), forming electron–hole pairs or excitons. These bound charge carriers are required to be separated into free charges within their lifetimes for participating in the reduction–oxidation reaction to generate superoxide and hydroxyl radicals. However, the charge recombination rate in ZnO is faster because there is no driving force for separating and mobilizing electrons and holes to the surfaces of ZnO

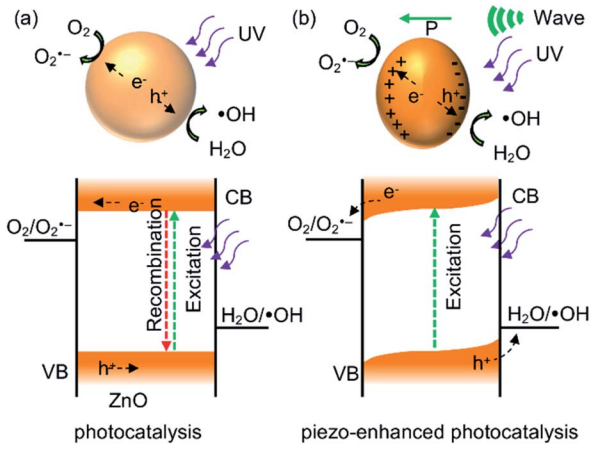

Fig. 8 Schematic representation of mechanisms in (a) photocatalysis and (b) piezo-enhanced photocatalysis of ZnO nanoparticles.

nanoparticles. However, for the dual stimulation by photon and ultrasonic wave on ZnO catalyst, the built-in electric field created by charge polarization provides driving force for both excitons excitation and excitons separation as shown in Fig. 8b. Due to the suppression in charge recombination by this internal field, there are more free charge carriers acting as oxidant and reductant simultaneously, thereby providing access to reactive species such as superoxide radical ($O_2^{\bullet -}$) and hydroxyl radicals ($\cdot$OH). Then, the degradation of organic dyes possibly involves to those reactive species. However, free charge carriers may be trapped at the surface states formed by the organic residues or surface defects, leading to reduction in reactive species. Therefore, removal of the surface residues is crucial for enhancing the dye degradation performance.

To investigate how these reactive species were involved in the process, several experiments were conducted. At first, degradation of MB was carried out in the presence of ZnO and different scavengers of the reactive species. The presence of $AgNO_3$ (electron scavenger) improves the catalytic activity. It can be explained by Ag^+ accepts an electron to generate silver which can serve as a cocatalyst in dye degradation. Indeed, Ag–ZnO composites are known to photocatalyze MB degradation.[53] The addition of *t*-butanol (hydroxyl radical scavenger) inhibits the photocatalytic activity. This result indicates the generation of hydroxyl radical is a responsible species for the dye degradation.

Conclusions

We reported a single-component ZnO nanoparticle catalyst, synthesized by surfactant-assisted precipitation at low temperature (60 °C), for dye wastewater treatment *via* piezo-enhanced photocatalysis. The applied mechanical force on ZnO nanoparticles was found to remarkably enhance photocatalytic degradation. After thoroughly characterizations by various spectroscopic techniques, it was found that organic surface residuals in as-synthesized ZnO hindered the photocatalytic degradation efficiency. Calcined ZnO nanoparticles showed better photocatalytic and piezo-enhanced photocatalytic performances. In addition, surface properties of ZnO shed light on catalytic activities and piezo-enhanced photocatalytic degradation mechanisms. Therefore, photocatalytic MB degradation efficiencies could be synergistically enhanced by the vibrational force with the low catalyst loading and shorter reaction time. Additionally, piezo-promoted photocatalyst does not only degrade cationic dye but also applicable for anion dye. This work demonstrated that single-component ZnO nanoparticle catalyst could be alternative to commonly used ZnO nanowires and nanosheets.

Conflicts of interest

The authors declare that they have no competing interests.

Acknowledgements

This work was financially supported by Chiang Mai University. YC, SY and PR thanks Development and Promotion of Science and Technology Talent Projects (DPST) through research fund for DPST graduates with first placements. The authors would like to acknowledge Dr Pimluck Kijjanapanich of Faculty of Engineering, Chiang Mai University.

Notes and references

1 J. L. Gomez and O. Tigli, Zinc oxide nanostructures: from growth to application, *J. Mater. Sci.*, 2013, **48**, 612–624.
2 Q. Zhang, C. S. Dandeneau, X. Zhou and C. Cao, ZnO nanostructures for dye-sensitized solar cells, *Adv. Mater.*, 2009, **21**, 4087–4108.
3 A. Naveed Ul Haq, A. Nadhman, I. Ullah, G. Mustafa, M. Yasinzai and I. Khan, Synthesis Approaches of Zinc Oxide Nanoparticles: The Dilemma of Ecotoxicity, *J. Nanomater.*, 2017, **2017**, 1–14.
4 P. Ruankham, D. Wongratanaphisan, A. Gardchareon, S. Phadungdhitidhada, S. Choopun and T. Sagawa, Full coverage of perovskite layer onto ZnO nanorods *via* a modified sequential two-step deposition method for efficiency enhancement in perovskite solar cells, *Appl. Surf. Sci.*, 2017, **410**, 393–400.
5 F. Yang, D.-W. Kang and Y.-S. Kim, Improved interface of $ZnO/CH_3NH_3PbI_3$ by a dynamic spin-coating process for efficient perovskite solar cells, *RSC Adv.*, 2017, **7**, 19030–19038.
6 F. Fleischhaker, V. Wloka and I. Hennig, ZnO based field-effect transistors (FETs): solution-processable at low temperatures on flexible substrates, *J. Mater. Chem.*, 2010, **20**, 6622–6625.
7 L. Wang, S. Liu, Z. Wang, Y. Zhou, Y. Qin and Z. L. Wang, Piezotronic Effect Enhanced Photocatalysis in Strained Anisotropic ZnO/TiO_2 Nanoplatelets *via* Thermal Stress, *ACS Nano*, 2016, **10**, 2636–2643.
8 X. Xu, Y. Jia, L. Xiao and Z. Wu, Strong vibration-catalysis of ZnO nanorods for dye wastewater decolorization *via* piezo-electro-chemical coupling, *Chemosphere*, 2018, **193**, 1143–1148.
9 M. Thepnurat, T. Chairuangsri, N. Hongsith, P. Ruankham and S. Choopun, Realization of Interlinked ZnO Tetrapod Networks for UV Sensor and Room-Temperature Gas Sensor, *ACS Appl. Mater. Interfaces*, 2015, **7**(43), 24177–24184.
10 S. A. Ansari, M. M. Khan, M. O. Ansari, J. Lee and M. H. Cho, Biogenic synthesis, photocatalytic, and photoelectrochemical performance of Ag–ZnO nanocomposite, *J. Phys. Chem. C*, 2013, **117**, 27023–27030.
11 V. Rajendar, C. H. Shilpa Chakra, B. Rajitha, K. Venkateswara Rao, M. Chandra Sekhar, B. Purusottam Reddy and S. H. Park, Effect of TWEEN80 on the morphology and antibacterial properties of ZnO nanoparticles, *J. Mater. Sci.: Mater. Electron.*, 2017, **28**, 3272–3277.
12 P. Petkova, A. Francesko, M. M. Fernandes, E. Mendoza, I. Perelshtein, A. Gedanken and T. Tzanov, Sonochemical coating of textiles with hybrid ZnO/chitosan antimicrobial nanoparticles, *ACS Appl. Mater. Interfaces*, 2014, **6**, 1164–1172.

13 C. Tian, Q. Zhang, A. Wu, M. Jiang, Z. Liang, B. Jiang and H. Fu, Cost-effective large-scale synthesis of ZnO photocatalyst with excellent performance for dye photodegradation, *Chem. Commun.*, 2012, **48**, 2858–2860.

14 S. G. Kumar and K. S. R. K. Rao, Zinc oxide based photocatalysis: tailoring surface-bulk structure and related interfacial charge carrier dynamics for better environmental applications, *RSC Adv.*, 2015, **5**, 3306–3351.

15 S. Lan, L. Liu, R. Li, Z. Leng and S. Gan, Hierarchical hollow structure ZnO: synthesis, characterization, and highly efficient adsorption/photocatalysis toward congo red, *Ind. Eng. Chem. Res.*, 2014, **53**, 3131–3139.

16 D. Lin, H. Wu, R. Zhang and W. Pan, Enhanced photocatalysis of electrospun Ag–ZnO heterostructured nanofibers, *Chem. Mater.*, 2009, **21**, 3479–3484.

17 M. Kubo, H. Fukuda, X. J. Chua and T. Yonemoto, Kinetics of Ultrasonic Degradation of Phenol in the Presence of Composite Particles of Titanium Dioxide and Activated Carbon, *Ind. Eng. Chem. Res.*, 2007, **46**, 699–704.

18 D. H. Wi, S. Y. Park, S. Lee, J. Sung, J. W. Hong and S. W. Han, Metal-semiconductor ternary hybrids for efficient visible-light photocatalytic hydrogen evolution, *J. Mater. Chem. A*, 2018, **6**, 13225–13235.

19 Y. Zhang, X. Huang and J. Yeom, A Floatable Piezo-Photocatalytic Platform Based on Semi-Embedded ZnO Nanowire Array for High-Performance Water Decontamination, *Nano-Micro Lett.*, 2019, **11**, 11.

20 Z. Wang, T. Hu, H. He, Y. Fu, X. Zhang, J. Sun, L. Xing, B. Liu, Y. Zhang and X. Xue, Enhanced H_2 Production of TiO_2/ZnO Nanowires Co-Using Solar and Mechanical Energy through Piezo-Photocatalytic Effect, *ACS Sustainable Chem. Eng.*, 2018, **6**, 10162–10172.

21 E. S. Nour, O. Nur and M. Willander, Zinc oxide piezoelectric nano-generators for low frequency applications, *Semicond. Sci. Technol.*, 2017, **32**, 64005.

22 W. Qian, K. Zhao, D. Zhang, C. R. Bowen, Y. Wang and Y. Yang, Piezoelectric Material-Polymer Composite Porous Foam for Efficient Dye Degradation *via* the Piezo-Catalytic Effect, *ACS Appl. Mater. Interfaces*, 2019, **11**, 27862–27869.

23 Y. Feng, H. Li, L. Ling, S. Yan, D. Pan, H. Ge, H. Li and Z. Bian, Enhanced Photocatalytic Degradation Performance by Fluid-Induced Piezoelectric Field, *Environ. Sci. Technol.*, 2018, **52**, 7842–7848.

24 W. Yang, Y. Yu, M. B. Starr, X. Yin, Z. Li, A. Kvit, S. Wang, P. Zhao and X. Wang, Ferroelectric Polarization-Enhanced Photoelectrochemical Water Splitting in TiO_2 –$BaTiO_3$ Core–Shell Nanowire Photoanodes, *Nano Lett.*, 2015, **15**, 7574–7580.

25 D. Hong, W. Zang, X. Guo, Y. Fu, H. He, J. Sun, L. Xing, B. Liu and X. Xue, High Piezo-photocatalytic Efficiency of CuS/ZnO Nanowires Using Both Solar and Mechanical Energy for Degrading Organic Dye, *ACS Appl. Mater. Interfaces*, 2016, **8**, 21302–21314.

26 X. Guo, Y. Fu, D. Hong, B. Yu, H. He, Q. Wang, L. Xing and X. Xue, High-efficiency sono-solar-induced degradation of organic dye by the piezophototronic/photocatalytic coupling effect of FeS/ZnO nanoarrays, *Nanotechnology*, 2016, **27**, 375704.

27 H. You, Z. Wu, Y. Jia, X. Xu, Y. Xia, Z. Han and Y. Wang, High-efficiency and mechano-/photo- bi-catalysis of piezoelectric-ZnO@ photoelectric-TiO_2 core–shell nanofibers for dye decomposition, *Chemosphere*, 2017, **183**, 528–535.

28 M. M. Hossain, B. C. Ku and J. R. Hahn, in *Applied Surface Science*, Elsevier B.V., 2015, vol. 354, pp. 55–65.

29 H. Shima, M. M. Hossain, I. Lee, S. Son and J. R. Hahn, Carbon–ZnO core–shell nanospheres: facile fabrication and application in the visible-light photocatalytic decomposition of organic pollutant dyes, *Mater. Chem. Phys.*, 2017, **185**, 73–82.

30 M. Law, L. E. Greene, J. C. Johnson, R. Saykally and P. Yang, Nanowire dye-sensitized solar cells, *Nat. Mater.*, 2005, **4**, 455–459.

31 E. Hosono, S. Fujihara, I. Honma and H. Zhou, The Fabrication of an Upright-Standing Zinc Oxide Nanosheet for Use in Dye-Sensitized Solar Cells, *Adv. Mater.*, 2005, **17**, 2091–2094.

32 X. Guo, Y. Fu, D. Hong, B. Yu, H. He, Q. Wang, L. Xing and X. Xue, High-efficiency sono-solar-induced degradation of organic dye by the piezophototronic/photocatalytic coupling effect of FeS/ZnO nanoarrays, *Nanotechnology*, 2016, **27**, 1–11.

33 J. Theerthagiri, S. Salla, R. A. Senthil, P. Nithyadharseni, A. Madankumar, P. Arunachalam, T. Maiyalagan and H.-S. Kim, A review on ZnO nanostructured materials: energy, environmental and biological applications, *Nanotechnology*, 2019, **30**, 392001.

34 J. Xiong, S. Xiong, Z. Guo, M. Yang, J. Chen and H. Fan, Ultrasonic dispersion of nano TiC powders aided by Tween80 addition, *Ceram. Int.*, 2012, **38**, 1815–1821.

35 S. K. Sehmi, S. Noimark, S. D. Pike, J. C. Bear, W. J. Peveler, C. K. Williams, M. S. P. Shaffer, E. Allan, I. P. Parkin and A. J. MacRobert, Enhancing the Antibacterial Activity of Light-Activated Surfaces Containing Crystal Violet and ZnO Nanoparticles: Investigation of Nanoparticle Size, Capping Ligand, and Dopants, *ACS Omega*, 2016, **1**, 334–343.

36 D. Ramimoghadam, M. Z. Bin Hussein and Y. H. Taufiq-Yap, Hydrothermal synthesis of zinc oxide nanoparticles using rice as soft biotemplate, *Chem. Cent. J.*, 2013, **7**, 136.

37 M. Zare, K. Namratha, K. Byrappa, D. M. Surendra, S. Yallappa and B. Hungund, Surfactant assisted solvothermal synthesis of ZnO nanoparticles and study of their antimicrobial and antioxidant properties, *J. Mater. Sci. Technol.*, 2018, **34**, 1035–1043.

38 H. Ding, Z. Zhao, G. Zhang, Y. Wu, Z. Gao, J. Li, K. Zhang, N. Pan and X. Wang, Oxygen vacancy: an electron-phonon interaction decoupler to modulate the near-band-edge emission of ZnO nanorods, *J. Phys. Chem. C*, 2012, **116**, 17294–17299.

39 A. Singh, K. Senapati, B. Satpati and P. K. Sahoo, Suppression of near band edge emission in specially engineered ZnO twin nanorods, *Phys. Chem. Chem. Phys.*, 2017, **19**, 14012–14019.

40 V. V. Khomyak, M. M. Slyotov, I. I. Shtepliuk, G. V. Lashkarev, O. M. Slyotov, P. D. Marianchuk and V. V. Kosolovskiy, Annealing effect on the near-band edge emission of ZnO, *J. Phys. Chem. Solids*, 2013, **74**, 291–297.

41 A. B. Djurišić and Y. H. Leung, Optical properties of ZnO nanostructures, *Small*, 2006, **2**, 944–961.

42 D. J. Qiu, H. Z. Wu, A. M. Feng, Y. F. Lao, N. B. Chen and T. N. Xu, Annealing effects on the microstructure and photoluminescence properties of Ni-doped ZnO films, *Appl. Surf. Sci.*, 2004, **222**, 263–268.

43 B. Panigrahy, M. Aslam, D. S. Misra, M. Ghosh and D. Bahadur, Defect-related emissions and magnetization properties of ZnO Nanorods, *Adv. Funct. Mater.*, 2010, **20**, 1161–1165.

44 R. Raji and K. G. Gopchandran, ZnO nanostructures with tunable visible luminescence: effects of kinetics of chemical reduction and annealing, *J. Sci. Adv. Mater. Devices*, 2017, **2**, 51–58.

45 Y. Gu, I. L. Kuskovsky, M. Yin, S. O'Brien and G. F. Neumark, Quantum confinement in ZnO nanorods, *Appl. Phys. Lett.*, 2004, **85**, 3833–3835.

46 M. Šćepanović, M. Grujić-Brojčin, K. Vojisavljević and T. Srećković, Defect induced variation in vibrational and optoelectronic properties of nanocrystalline ZnO powders, *J. Appl. Phys.*, 2011, **109**, 34313.

47 M. J. Al-Saadi, S. H. Al-Harthi, H. H. Kyaw, M. T. Z. Myint, T. Bora, K. Laxman, A. Al-Hinai and J. Dutta, Influence of Atomic Hydrogen, Band Bending, and Defects in the Top Few Nanometers of Hydrothermally Prepared Zinc Oxide Nanorods, *Nanoscale Res. Lett.*, 2017, **12**, 22.

48 C. Belkhaoui, N. Mzabi, H. Smaoui and P. Daniel, Enhancing the structural, optical and electrical properties of ZnO nanopowders through (Al + Mn) doping, *Results Phys.*, 2019, **12**, 1686–1696.

49 C. Belkhaoui, N. Mzabi, H. Smaoui and P. Daniel, Enhancing the structural, optical and electrical properties of ZnO nanopowders through (Al + Mn) doping, *Results Phys.*, 2019, **12**, 1686–1696.

50 Y. Zuo, S. Ge, Z. Chen, L. Zhang, X. Zhou and S. Yan, Morphology, optical and magnetic properties of $Zn_{1-x}Ni_xO$ nanorod arrays fabricated by hydrothermal method, *J. Alloys Compd.*, 2009, **470**, 47–50.

51 S. Zhu and D. Wang, Photocatalysis: Basic Principles, Diverse Forms of Implementations and Emerging Scientific Opportunities, *Adv. Energy Mater.*, 2017, 7(23), 1700841.

52 S. Wang, Z. Wu, J. Chen, J. Ma, J. Ying, S. Cui, S. Yu, Y. Hu, J. Zhao and Y. Jia, Lead-free sodium niobate nanowires with strong piezo-catalysis for dye wastewater degradation, *Ceram. Int.*, 2019, **45**, 11703–11708.

53 M. J. Height, S. E. Pratsinis, O. Mekasuwandumrong and P. Praserthdam, Ag–ZnO catalysts for UV-photodegradation of methylene blue, *Appl. Catal., B*, 2006, **63**, 305–312.